In-Duct Measurements: Modal Identification of Ducted Sources

Stefan Sack and Mats Åbom
KTH - The Royal Institute of Technology
The Marcus Wallenberg Laboratory for Sound and Vibration Research,
SE- 100 44 Stockholm

Contents

1.0 INTRODUCTION

Two-port modelling is commonly applied in engineering applications with the aim of determining the scattering behaviour of aeroacoustic elements in connected duct and pipe systems with flow, and to extract the reflection-free source vector from measurement data [1–5]. That data can be used to predict scattering and sound-emission for sophisticated aeroacoustic systems for low frequencies (plane waves), without measuring or simulating them as a whole. The main assumption being that the studied system is linear and time-invariant and that the division in sub-systems is made in such a way, that the inflow conditions to each element correspond to the reference case used for the determination of the two-port data. The overall sound-emission evoked by interconnected components can eventually be predicted with fairly low effort, which is exploited to design systems and abate noise. The two-port characteristics can furthermore be used to predict interactions between the hydrodynamic field and the sound field, e.g. to find critical setups for whistling [6].

As discussed by Boden and Åbom [1], multi-port models of higher order can be used to treat cases with three or more connected ducts with plane waves, e.g., a T-junction as in Ref. [7], or ducts with higher order modes. An early example of multi-port work involving higher order modes is Lavrentjev and Åbom [8]. More recent work has been done by Trabelsi et al. [9] on obstacles in rectangular ducts. Sitel et al. investigated the scattering of discontinuities in circular ducts for multi-ports of the order 5, but concentrated on the influence of the positions of the external sources and their over-determination. This work has been applied by Taktak et al. to the impedance measurement of induct liners for higher order modes [10].Another recent work is Newman et al. [11] who applied the theory proposed in Ref. [8] for multi-port testing to a case with three propagating modes. The studied object was a low speed fan and the purpose to obtain better source data by a standard method (e.g. ISO 5136). In addition an error analysis was presented for the wave decomposition applying the methods presented in Ref. [12]. Compared to the plane wave range, however, the amount of published work is limited with the main reason being the rapidly increasing complexity of experiments and post-processing involving higher-order modes. It can also be noted that most of the published work on higher order multi-ports is experimental. Nevertheless, the rapidly growing accessibility of numerical computations (e.g., compressible flow simulations [13]) for aeroacoustic induct elements opens the possibility to also apply multi-port models to numerical data.

The characteristic parameters of a multi-port are usually ascertained in two steps [14]. First, independent sound fields are excited by external sources. Pressure sensors located upstream and downstream are utilised to decompose these sound fields into incident and outgoing wave-modes, leading to transmission and reflection coefficients of the system. To conduct the decomposition, an analytical solution of the wave equation is used to map a superposition of propagating modes to the measured pressure points. This semi-analytical approach requires the knowledge of the mode shapes along a cross-section in the duct and the propagation speed of the modes, namely the complex wave number.

In a second step, these scattering parameters are applied to extract reflection-free source strength data from acoustic records of the noise emitted by the system. The quality of the results achieved with this method is highly dependent on the experimental setup, namely the pressure sensor and source positions. Åbom and Bodèn proposed criteria for the axial microphone separation for plane wave two-port characterisations, based on singular decomposition matrices [15]. In later studies, extensions to a higher order mode decomposition are derived [16], assuming that the mode shapes could be separated in a single sensor-section, using wall mounted pressure sensors. To separate incident from outgoing modes, a second sensor-section is used, that has to satisfy the sampling condition from the two microphone method. This approach is, however, sensitive for mode coupling at certain frequencies and results in ill-conditioned decomposition matrices. Here, we extend the investigations of Åbom [16] and proposes guidelines for sensor and source placing at arbitrary positions on

the channel walls in order to achieve well-conditioned decomposition matrices and to facilitate the experimental rig design. As a new approach, singularities caused by couplings within two dissimilar modes are investigated using vector-base calculations. Furthermore, we show a method to evaluate the quality of certain sensor spacing by utilising the condition number of the projected modal matrix. This approach has been successfully applied by Gerhold et al. [17], but only for the two-microphone method. Gerhold optimises microphone arrays in rectangular ducts, based on the condition number of the highest frequency. Such a single-frequency method estimates the measurement quality but fails on narrow-band singularities evoked by mode coupling. Here, the condition number is used over the entire measurement spectrum to optimise the sensor configuration. However, such optimisation is complicated due to the high number of parameters. We introduce a genetic algorithm into the actual optimisation problem. To show the improvement in terms of uncertainty propagation through the modal decomposition, a Monte-Carlo simulation is performed on simulated scattering data for the optimised and non-optimised setup. This has been done by Schultz et al. [18] but only for the two-microphone method. Schultz showed that the Monte Carlo Method treats uncertainties with higher accuracy than the linear multivariate uncertainty analysis.

The same criteria established for the microphone sections might be applied to the design of the source arrays. Since sources for real measurements commonly require more mounting space, non-singular setups cannot generally be guaranteed. We eradicate this detriment by introducing source over-determination. Holmberg et al. [3] as well as Sitel et al. [19] have empirically shown the positive effect of source over-determination on the characterisation of acoustic two-ports.

In order to minimise the uncertainty in the decomposition technique, a precise knowledge of the mode-shapes and complex wave numbers is mandatory and there exist various models to compute both as eigen-solutions of simplified Navier-Stokes Equations. Models of different levels of simplification will be used here for the wave decomposition. First, a none-dissipative model, taking only convective flow into account. However, Allam and Åbom showed that thermo-viscous dissipation is relevant for acoustic in-duct propagation [20]. We, hence, compare the classical Kirchhoff theory extended for in-duct flow with an eigen-value solution for higher order modes obtained by Dokumaci [21].

Firstly, we introduce the multi-port approach and the modal decomposition, which is a review of the existing literature and theory (Section 2.0). Secondly, we describe the general method to determine multi-port data from measurements and simulations (Section 3.0) and point out difficulties in the test-rig design, namely finding appropriate source and sensor positions (Section 4.0). We discuss frequencies with singular mode decompositions due to mode coupling and show how to evaluate and to optimise a test setup applying the Monte Carlo Simulation and Genetic Algorithms (Section 5.0). In the 'results' section, we apply the theory to measurements and computations of two test cases. In Section 6.5, the scattering matrix of a straight duct of the diameter 150 mm is measured between 500 Hz and 3000 Hz, which contains the cut-on of 6 duct-modes. We use the genetic algorithm to optimise the measurement setup and the Monte Carlo Method to evaluate the enhancement. We apply different wave number models to the decomposition in order to show possible differences in the results (Section 6.6). We use the full-wave decomposition to precisely determine the temperature and mean-flow velocity of the measurement (Section 6.7). Finally, we apply the multi-port procedure to compute the acoustic scattering from an orifice, using the Finite Element Method. We use highly over-determined decomposition matrices in order to extract the complex mode amplitudes from grid data and we compare the numerical results with experimental data (Section 6.8).

2.0 THEORETICAL INVESTIGATIONS

2.1 Mode Decomposition in Ducts with Flow

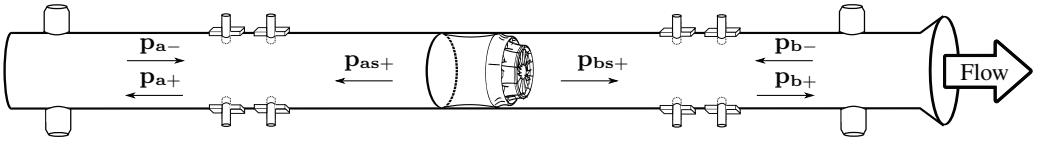

Figure 1: An illustration of an acoustic multi-port. The vectors p_+ and p_- are acoustic pressure perturbations in outgoing and incident direction, S is the scattering matrix and p_{s+} the source vector. The indices a and b denote the downstream and upstream side of the multi-port.

Aeroacoustic duct elements can be described with multi-port models [1, 22]. This approach is advantageous as sophisticated duct systems can be partitioned in ascertainable subcomponents. These components are defined by their transmission and reflection properties of acoustic wave modes and their capability to excite acoustic fields. We denote the analytical eigen-solution of a wave equation, e.g. the Helmholz Equation as an acoustic mode. A subcomponent in a duct, as in Figure 1, can mathematically be described in the frequency domain as

$$\mathbf{p}_+(\omega) = \quad \mathbf{S}(\omega)\, \mathbf{p}_-(\omega) + \mathbf{p}_{s+}(\omega) \quad , \tag{1}$$

with

$$\mathbf{p}_\pm = \begin{bmatrix} \mathbf{p}_{a\pm} \\ \mathbf{p}_{b\pm} \end{bmatrix}, \quad \mathbf{p}_{s+} = \begin{bmatrix} \mathbf{p}_{as+} \\ \mathbf{p}_{bs+} \end{bmatrix} \tag{2}$$

and $\mathbf{p}(\omega)_\pm \in \mathbb{C}^{[2N\times 1]}$ are the complex vectors of modal pressure amplitudes for a certain angular frequency ω. The indices $-$ and $+$ indicate the incident and outgoing direction of the modes and the indices a and b denote the downstream and upstream side of the test-object. Equation 1 is only valid for linear and time invariant systems. Linearity applies for sound pressure levels of less than 150 dB [22] and time invariance implies that the system properties e.g., the speed of sound, temperature, geometry, and boundary conditions are constant.

At an angular frequency ω a number of N modes are propagating which we denote as cut-on modes. The scattering matrix $\mathbf{S} \in \mathbb{C}^{[2N\times 2N]}$ contains the transmission and reflection of all N modes at the inlet and the outlet, whereas in our notation the elements of its main diagonal describe pure reflection of single modes, the N-th minor diagonal describes pure transmission, and the remaining elements describe scattering of acoustic pressure between dissimilar modes (Figure 2). The number of modes N are chosen to correspond to the modes

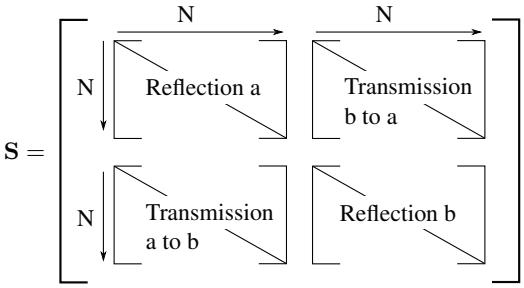

Figure 2: Schematic of the contents of the scattering matrix. The downstream and upstream side of the multi-port is denoted with a and b, respectively.

that are cut-on. In principle, cut-off modes can be included which can be important, e.g. for in-duct acoustic holography [5].

The source vector $\mathbf{p}_{s+} \in \mathbb{C}^{[2N\times 1]}$ contains the sound waves which are generated by the element itself under reflection-free conditions. We refer to the scattering matrix as passive part and to the source vector as active part of the multi-port, where the aim of a full multi-port analysis is to determine such characteristic properties. A key step, thereby, is to determine the complex mode amplitudes $\mathbf{p}(\omega)_{\pm}$ in both propagating directions at the multi-port inlet and outlet. This is done by applying a modal decomposition technique to the acoustic fields which are sampled at n spatial positions up- and downstream of the subcomponent, where $n \geq 2 \times N$.

We introduce a vector $\mathbf{\Omega}^{[1\times N]}$ containing all cut on modes in a circular duct sorted by ascending cut-on frequencies such as

$$\mathbf{\Omega} = [(0,0)\,, (1,0)\,, (\text{-}1,0)\,, (2,0)\,, (\text{-}2,0)\,, (0,1),\ \ldots] \quad , \tag{3}$$

where for a mode (m,n) m is the azimuthal mode order and n is the radial mode order. A mode of the order i will now be referred to the i-th element of $\mathbf{\Omega}$, where Ω_1 is the plane wave mode.

We, furthermore, define a vector $\mathbf{\Upsilon}^{[1\times n]}$ for the n sensor points which are used to sample the sound-pressure field such that

$$\mathbf{\Upsilon} = [(\Phi_0, z_0, r_0), (\Phi_1, z_1, r_1), (\Phi_2, z_2, r_2), \ldots, (\Phi_n, z_n, r_n)] \tag{4}$$

and Υ_j contains the cylindrical coordinates of the j-th sensor point. The denotion 'sensor point' will not restrict the method to measurement data but can also be understood as a sensoring-point in a numerical grid.

We can write the acoustic pressure at each sensor point as superposed eigen-modes

$$p_j = \sum_{i=1}^{N} p_{+i}\Psi_{+j,i}T_{+j,i} + \sum_{i=1}^{N} p_{-i}\Psi_{-j,i}T_{-j,i}, \tag{5}$$

where $\Psi_{\pm}$ denotes the mode shape within a duct cross-section and $T_{\pm}$ describes the axial wave propagation relative to a reference point. Here, $+$ and $-$ denote the upstream and downstream direction of the sound propagation. Both, $\Psi_{\pm}$ and $T_{\pm}$ are functions of the sensor point position and the propagating mode. We assume a rigid walled straight duct and fully developed plug flow that causes, due to its axial symmetry, similar mode shapes in both propagation directions $\Psi_+ = \Psi_- = \Psi$ and we can express the functions $\Psi_{j,i}$ and $T_{j,i}$ as [23]

$$T_{\pm j,i} = \quad exp(-\mathbf{i} z_j k_{i\pm}) \tag{6}$$

$$\begin{aligned} \Psi_{j,i} &= \quad \tilde{C}_i J_{m_i}(\kappa_i\, r_j)\, exp(\mathbf{i}\Phi_j m_i) \\ &= \quad C_{j,i}\, exp(\mathbf{i}\Phi_j m_i) \qquad , \end{aligned} \tag{7}$$

where $(\Phi_j, z_j, r_j) = \Upsilon_j$, $(m_i, n_i) = \Omega_i$, $k_{i\pm}$ is the wave number, and $C_{j,i}$ is the radial mode-shape as a function of J_{m_i}, the Bessel-function of the first kind and order m_i, a mode-depending normalisation factor $\tilde{C}_i$, and the m_i-th root of the derivative of the Bessel-function κ_i such that $J'_{m_i}(\kappa_i\, R) = 0$ for the duct radius R. Considering all sensor points, we can rewrite Equation 5 in matrix notation

$$\mathbf{p}(\omega) = \mathbf{M}(\omega)\, \mathbf{p}_{\pm}(\omega) \quad , \tag{8}$$

where $\mathbf{p} \in \mathbb{C}^{[n\times 1]}$ is the vector of sampled pressures and $\mathbf{M} \in \mathbb{C}^{[n\times 2N]}$ is the modal matrix. The modal matrix maps the superposition of complex mode vectors to the measured pressure-points. Taking into account convective flow effects, we can split $\mathbf{M}$ into a pair of modal matrices

$$\mathbf{M} = \quad [\mathbf{M}_+ \quad \mathbf{M}_-] \quad . \tag{9}$$

Following from Equation 5, we can rewrite the convective sub-matrices to

$$\mathbf{M}_{\pm} = \overset{\text{sensors}}{\downarrow} \overbrace{\begin{pmatrix} \Psi_{1,1}T_{\pm 1,1} & \Psi_{1,2}T_{\pm 1,2} & \cdots & \Psi_{1,N}T_{\pm 1,N} \\ \Psi_{2,1}T_{\pm 2,1} & \Psi_{2,2}T_{\pm 2,2} & \cdots & \Psi_{2,N}T_{\pm 2,N} \\ \vdots & \vdots & \ddots & \vdots \\ \Psi_{n,1}T_{\pm n,1} & \Psi_{n,2}T_{\pm n,2} & \cdots & \Psi_{n,N}T_{\pm n,N} \end{pmatrix}}^{\text{modes} \rightarrow}, \tag{10}$$

where the j-th row corresponds to the j-th sensor point and the i-th column to the mode of the i-th order.

2.2 Wave Number Estimations

A good estimate of the complex wave number $k_{i\pm}$ in Equation 6 is crucial for reliable wave decomposition. In the literature, there are wave number estimates of different complexity, depending on the included mechanisms of dissipation. In Section 6.6, three different formulations are compared. First, a non-dissipative wave number model for sound propagation in ducts with convective flow is used [23]

$$k_{i\pm} = \pm \frac{\omega}{c} \frac{\sqrt{1 - (\kappa_i c/\omega)^2 (1 - M^2)} \mp M}{1 - M^2} \quad , \tag{11}$$

where M is the Mach-number of the mean-flow and c is the speed of sound inside the duct. Equation 11, however, does not account for dissipative effects. In addition, we use the Kirchhoff formulation, which accounts for thermo-viscous effects [20]. We define a correction parameter K_0 which we multiply with the wave number in Equation 11

$$K_0 = 1 + \frac{1 - \mathbf{i}}{\sqrt{2}s} \left(1 + \frac{(\gamma - 1)}{\xi} \right) - \frac{\mathbf{i}}{s^2} \left(1 + \frac{(\gamma - 1)}{\xi} - \frac{(\gamma^2 - \gamma)}{2\xi^2} \right). \tag{12}$$

Here, γ is the specific heat ratio, $\xi^2 = \mu C_p / \kappa_{th}$ is the Prandtl-number, $s = r\sqrt{\rho_0 \omega / \mu}$ is the shear wave number, μ is the dynamic viscosity, ρ_0 is the quiescent density, κ_{th} is the thermal conductivity, C_p is the specific heat coefficient of the fluid, and r is the duct radius. The resulting complex wave number is a function of the fluid properties, but the derivation assumes plane wave propagation only and we expect inaccuracy for higher order modes.

We finally use Dokumaci's dissipation model, which gives a formulation for thermo-viscous dissipation of higher order acoustic modes in presence of mean flow by iteratively solving the eigen-value problem of a dissipative wave equation. A more detailed description of this method can be found in Ref. [21].

3.0 MULTI-PORT EDUCTION IN MEASUREMENTS AND COMPUTATIONS

The decomposition method presented here represents a general post-processing approach for acoustic pressure and is not restricted to the origin of the pressure data. The classical application, however, is the scattering and source characterisation especially of acoustic two-ports from measurement data [3]. Those measurements are usually carried out with a low number of sensor points and the sensor positions are restricted to the channel walls to guarantee the undisturbed inflow to the test objects and to minimise local flow noise in the measured signals. The modal decomposition of measurement data scales down to a matrix inversion of $\mathbf{M}$ (see Equation 8), which is usually square or only slightly overdetermined. The fact that the stability of this method highly depends on

the invertibility of the modal decomposition matrix engender challenges in the test-rig design, i.e. in the sensor and source placing.

Increasing interest in numerical computations and higher capability to generate and access large data sets opens new fields of applications for multi-port characterisation techniques. The decomposition of numerical data brings a number of advantages compared to the empirical approach. Admittedly, the computed time samples are still much shorter than data gained from measurements. However, a plethora of sensoring-points is accessible, even inside the channel cross-sections. The decomposition matrix is hence highly over-determined and guarantees a stable matrix inversion. Furthermore, in computations we can disable all disturbing effects e.g. thermo-viscous damping, fluctuations in temperature and flow-velocity, and structural vibrations of the test-rig, which usually complicate measurements.

The general approach to gain multi-port data from measurements and computations is similar. However, simulations and measurements engender different challenges and require adapted procedures, which we describe in detail for measurements in Section 3.1 and for computations in Section 3.2.

3.1 Multi-Port Eduction Using Measurement Data

The pressure field generated by an aeroacoustic source that we sample in experiments is always a superposition of the sound created by the source itself, external sound which is scattered inside the test-rig, and hydrodynamic pressure fluctuations from the flow field. A multi-port eduction, therefore, involves two steps [8]. First, the system scattering is isolated from Equation 1. Artificial acoustic loads are generated by external sound sources at the upstream and downstream side of the test object to measure the transmission and reflection at the inlet and at the outlet. Those sound fields have to be uncorrelated to the source of the test object so that we can neglect the source vector $\mathbf{p}_{s+}$ in Equation 1. In addition, the signal used to excite the external sources can be used as a reference to improve the signal-to-noise ratio in the data [8]. We compute the scattering matrix

$$\mathbf{p}_{+}\mathbf{p}_{-}^{-1} = \mathbf{S} \quad , \tag{13}$$

where $(\ldots)^{-1}$ denotes the (pseudo-) inverse. Note that here, other than in Equation 1, $\mathbf{p}_{+}$ and $\mathbf{p}$ are matrices which have the different external acoustic fields as columns and the complex mode amplitudes of the decomposed fields as rows. The scattering matrix $\mathbf{S}$ has the dimension $2N \times 2N$ and we, therefore, need N mathematically linear independent complex mode vectors from decomposed external sound fields upstream and downstream to solve all its coefficients. Depending on the test-object, we might reduce the number of necessary sound fields, e.g. by assuming symmetry in the circumferential mode pairs or in upstream and downstream direction.

Furthermore, we can use the same sound fields to solve for the reflection coefficients of the test-rig terminations

$$\mathbf{R} = \begin{bmatrix} \mathbf{R}_a & \mathbf{0} \\ \mathbf{0} & \mathbf{R}_b \end{bmatrix} = \begin{bmatrix} \mathbf{p}_{a-}\,\mathbf{p}_{a+}^{-1} & \mathbf{0} \\ \mathbf{0} & \mathbf{p}_{b-}\,\mathbf{p}_{b+}^{-1} \end{bmatrix}, \tag{14}$$

where we have to use the sound fields which are excited at the opposite end of the test object, i.e. the downstream excitation for the upstream reflection and vice versa. This may lead to difficulties as for strongly reflecting or absorbing test-objects, e.g. mufflers, the sound-pressure level can be too weak to be clearly recognised in the hydrodynamic noise on the other side of the test object. For such cases, it might be necessary to arrange a separate measurement of the reflection removing the test object [2].

In a second step, the source vector can be isolated from plain 'listening' data, without external sources. However, this approach engenders two problems. First, the aeroacoustic source signal is usually covered by

strong hydrodynamic noise. Such fluctuations are eliminated from the passive measurement by correlating the sensor signal to the driving signal of the external sources. In active measurements, however, we do not apply external sources and we usually do not have access to any reference signal correlated to the sources either, which is only possible when measuring on the harmonics from periodic machines [1]. Using plain auto-spectra of the microphone signals, however, leads to much higher pressure levels, blurred mode-amplitudes, and corrupted phase information.

Another problem in active measurements is the reflections induced by the test-rig terminations. Those reflections superpose with the actual acoustic source and cause errors in the solution of the source vectors. A multi-port eduction which does not account for internal test-rig reflection generates mode-vectors which are measurement-specific and hence not comparable with the data gained from different assemblies, e.g. computations or different test-rigs.

We use Equation 14 to rearrange Equation 1 to

$$\mathbf{p}_{s+} = [\mathbf{E} - \mathbf{S}\,\mathbf{R}]\,\mathbf{p}_{+} \quad , \tag{15}$$

where $\mathbf{E}$ denotes the unit matrix. We define the modal decomposition for the inlet and outlet of the test-object

$$\begin{bmatrix} \mathbf{p}_a \\ \mathbf{p}_b \end{bmatrix} = \begin{bmatrix} \mathbf{M}_a & \mathbf{0} \\ \mathbf{0} & \mathbf{M}_b \end{bmatrix} \begin{bmatrix} \mathbf{p}_{a+} \\ \mathbf{p}_{a-} \\ \mathbf{p}_{b+} \\ \mathbf{p}_{b-} \end{bmatrix} = \mathbf{M}\,\mathbf{p}_{\pm} \quad . \tag{16}$$

We further introduce a matrix $\mathbf{T}$, such that

$$\mathbf{p} = \mathbf{M}\,\mathbf{T}\,\mathbf{p}_{+} \quad , \tag{17}$$

with

$$\mathbf{T} = \begin{bmatrix} \mathbf{E} & \mathbf{0} \\ \mathbf{R}_a & \mathbf{0} \\ \mathbf{0} & \mathbf{E} \\ \mathbf{0} & \mathbf{R}_b \end{bmatrix} \quad . \tag{18}$$

Inserting Equation 17 into Equation 15, we can finally derive an expression for the modal source vector that only depends on measurable values

$$\begin{aligned} \mathbf{p}_s &= [\mathbf{E} - \mathbf{S}\,\mathbf{R}]\,(\mathbf{M}\mathbf{T})^{-1}\,\mathbf{p} \\ &= \mathbf{C}\,\mathbf{p} \quad . \end{aligned} \tag{19}$$

The formulation of Equation 19 accounts for the internal reflection of the test-rig, which results in reflection-free and hence test-rig independent source-vectors. We, furthermore, halved the degree of freedom in the modal decomposition and reduced the number of necessary sample points as we only decompose $\mathbf{p}_+$, which enables us to conduct two independent wave-decompositions which can be correlated to reduce uncorrelated, hydrodynamic noise. We can separate our $2N$ sensor positions in two groups (1 and 2) trying to maximise the distance between the microphone pairs and define the pressure vectors $\mathbf{p_1}$ and $\mathbf{p_2}$. We can now introduce the source cross-spectrum $\mathbf{G}_s$

$$\mathbf{G}_s = \mathbf{p}_{s1}\,\mathbf{p}_{s2}^{c} = \mathbf{C}_1\mathbf{p}_1\,(\mathbf{C}_2\mathbf{p}_2)^{c} \tag{20}$$

$$= \mathbf{C}_1\mathbf{p}_1\,\mathbf{p}_2^{c}\mathbf{C}_2^{c} \quad , \tag{21}$$

where $(\ldots)^c$ denotes the complex conjugated and transpose. Equation 19 and Equation 21 extend the investigations of Lavrentjev and Åbom [14] for two-sided multi-ports of arbitrary mode order.

We can conclude that the modal decomposition is a key method in both, the active and the passive measurement. As presented in, its quality mainly relies on the sensor and source position. The focus here is on the passive characterisation to demonstrate our methods and how to evaluate a given sensor and source configuration. However, an example showing the extraction of source data of an axial compressor using this theory can be found in Ref. [2].

3.2 Multi-Port Eduction Using Numerical Data

In computation, models with very low internal reflections can be realised, e.g. by adding sponge-layers or perfectly matched layers to the duct terminations [6]. This enables us,as opposed to measurements, to extract the source data directly from a single computation. One example is presented by Alenius [13], where the source data of a circular orifice plate in a low Mach-number flow is extracted from compressible flow (LES) simulations.

The scattering for duct elements can also be obtained using compressible flow computations or Large Eddy Simulations as shown by Alenius [13] and Lacombe [24]. These papers treated 2-ports and the plane wave range, but since large eddy simulations are computationally very heavy, it is not ideal to extend the approach to higher order modes. Kierkegaard et al. [6] demonstrated a simplified method in order to compute the scattering of an induct orifice plate, using Linearised Navier-Stokes Equations in the frequency domain. The advantage of this approach is that the steady flow field could be computed separately in a first step and is than coupled to the acoustics, which reduces the degree of freedom for the acoustic computation significantly. However, this work was only conducted for the plane wave mode in a two-dimensional computation. Later, we demonstrate the decomposition method on a three-dimensional grid to account for higher order modes as well. We apply the mode decomposition directly to the computational data, which due to the Moore-Penrose pseudo inverse of the highly over-determined decomposition matrix $\mathbf{M}$ behaves like a least square filter on the numeric data. To focus on the method described and not on numerical subtleties, the computation is conducted without mean flow, which simplifies the computational effort considerably. As the duct diameter is large, compared to the acoustic boundary layers, we neglected thermal-viscous effects. As governing equations, we chose the linear continuity and momentum equation

$$-\mathbf{i}\omega\mathbf{p} + \rho_0 c^2 \nabla \cdot \mathbf{v} = 0 \tag{22}$$

$$-\mathbf{i}\omega\rho_0\mathbf{v} = \rho_0\mathbf{F} - \nabla\mathbf{p}, \tag{23}$$

with the pressure and velocity perturbation in frequency domain $\mathbf{p}$ and $\mathbf{v}$, a source force $\mathbf{F}$, and the speed of sound in the medium c. With regard to boundaries, we use slip boundary conditions and zero normal velocity

$$\mathbf{u} \cdot \mathbf{n} = 0 \quad , \tag{24}$$

where $\mathbf{n}$ is the unit vector normal to the duct walls. The acoustic excitation is accomplished with pure mode excitations in a cross-section close to the duct inlets and outlets. The sources are realised as distributed forces in a sub-area of the computational domain upstream and downstream of the test-object. The force distribution over the duct cross-section is computed with Equation 7 which results in the higher order mode-shapes in Figure 3.

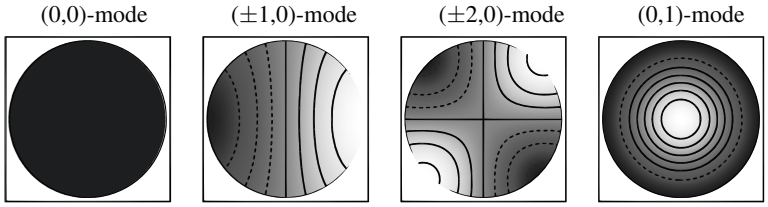

Figure 3: Real part of the force to excite an (m,n)-mode.

4.0 TEST-RIG DESIGN FOR ACCURATE MULTI-PORT MEASUREMENTS

In Section 2.0, we described the modal decomposition technique, which is a key method in the multi-port eduction for both properties, the scattering matrix and the source vector. It involves the matrix inversion of the modal matrix $\mathbf{M}$ which, therefore, becomes of particular interest for stability analyses of the modal decomposition. As shown in Equation 10, its values are functions of the acoustic mode shapes and wave numbers and the positions of the sensor points. Unfavourable axial and azimuthal sensor separation can cause linear dependent matrix rows or columns in $\mathbf{M}$, which disturb the decomposition and amplify uncertainties. Such singularities were investigated by Åbom et al. [16]; However, the study focusses on axial sensor separation. Singular decompositions were found for frequencies whose half-wave length corresponds to the axial sensor separation in the two-microphone method. In this section, we generalise that result for an arbitrary number of sensors and azimuthal sensor positions.

4.1 Conditions for Non-singular Sensor Spacing

The i-th column of the modal matrix $\mathbf{M}$ represents the complex distribution of the i-th mode at the sensor positions in $+$ direction for $i \leq N$ and the $(i-N)$th mode in $-$ direction for $i > N$. The modal decomposition becomes singular, if columns of $\mathbf{M}$ are linear dependent. This can be interpreted as coupling of the mode shapes (or waves) at the microphone positions and we refer to it as mode coupling.

We want to investigate the coupling of $K \leq 2N$ arbitrary modes (waves) and we separate the corresponding columns from the modal matrix which results in a sub-matrix $\mathbf{D}^{[n\times K]}$

$$\mathbf{D} = \overset{\text{sensors}}{\downarrow} \overset{\text{modes}}{\longrightarrow} \begin{pmatrix} \Psi_{1,i_1}T_{1,i_1} & \Psi_{1,i_2}T_{1,i_2} & \cdots & \Psi_{1,i_K}T_{1,i_K} \\ \Psi_{2,i_1}T_{2,i_1} & \Psi_{2,i_2}T_{2,i_2} & \cdots & \Psi_{2,i_K}T_{2,i_K} \\ \vdots & \vdots & \ddots & \vdots \\ \Psi_{n,i_1}T_{n,i_1} & \Psi_{n,i_2}T_{n,i_2} & \cdots & \Psi_{n,i_K}T_{n,i_K} \end{pmatrix}, \tag{25}$$

where $i_{1\ldots K}$ is the mode order of the arbitrary modes. Mode coupling occurs if the columns of that sub-matrix $\mathbf{D}$ are linear dependent

$$\sum_{i=1}^{K} a_i \mathbf{D}_i = \mathbf{0}, \tag{26}$$

for at least one non-trivial constant a_i and $\mathbf{D}_i$ is the i-th column of $\mathbf{D}$. As the values in the column-vector $\mathbf{D}_i$ are complex functions of the wave number, the mode-shapes, and the sensor positions a general solution of Equation 26 may be inappropriate for a high number of modes. However, we can yield a useful simplification

if we consider the coupling of two modes

$$\mathbf{D}_{i_1} = a\,\mathbf{D}_{i_2} \quad . \tag{27}$$

If Equation 27 has a non-trivial solution, the chosen sensor spacing is singular. We can easily argue that also any pair of values in $\mathbf{D}_{i_1}$ has the same non-trivial solution, i.e.

$$\begin{bmatrix} D_{j_1,i_1} \\ D_{j_2,i_1} \end{bmatrix} = a \begin{bmatrix} D_{j_1,i_2} \\ D_{j_2,i_2} \end{bmatrix} \tag{28}$$

with the two sensor points j_1 and j_2. This leads us to a condition for non-singular sensor separation

$$\left| \begin{pmatrix} \Psi_{j_1,i_1} T_{j_1,i_1} & \Psi_{j_1,i_2} T_{j_1,i_2} \\ \Psi_{j_2,i_1} T_{j_2,i_1} & \Psi_{j_2,i_2} T_{j_2,i_2} \end{pmatrix} \right| \neq 0 \quad , \tag{29}$$

where $|\cdot|$ denotes the determinate. Note, that Equation 29 has to be fulfilled for at least one combination of sensor points to avoid mode coupling for the modes i_1 and i_2. We insert Equation 6 and 7 into Equation 29

$$\begin{aligned} &C_{j_1,i_1} C_{j_2,i_2} \mathbf{e}^{\mathbf{i}(\phi_{j_1} m_{i_1} + \phi_{j_2} m_{i_2} - k_{i_1} z_{j_1} - k_{i_2} z_{j_2})} \\ &= C_{j_1,i_2} C_{j_2,i_1} \mathbf{e}^{\mathbf{i}(\phi_{j_1} m_{i_2} + \phi_{j_2} m_{i_1} - k_{i_2} z_{j_1} - k_{i_1} z_{j_2})}, \end{aligned} \tag{30}$$

which can be rewritten as

$$\mathbf{e}^{\mathbf{i}\psi} = Q, \qquad \psi, Q \in \mathbb{C}, \tag{31}$$

with

$$\begin{aligned} \psi &= (\phi_{j_1} - \phi_{j_2})\,(m_{i_1} - m_{i_2}) + (z_{j_1} - z_{j_2})\,(k_{i_1} - k_{i_2}), \\ Q &= \frac{C_{j_1,i_2}}{C_{j_1,i_1}} \frac{C_{j_2,i_1}}{C_{j_2,i_2}} \quad . \end{aligned} \tag{32}$$

For wall mounted sensors, $C_{j_1,i} = C_{j_2,i}$ and hence $Q = 1$ and Equation 31 gives us a solution for mode coupling due to insufficient axial and circumferential sensor positions

$$(\phi_{j_1} - \phi_{j_2})\,(m_{i_1} - m_{i_2}) + (z_{j_1} - z_{j_2})\,(k_{i_1} - k_{i_2}) = 2\pi l, \tag{33}$$

with $l \in \mathbb{Z}$. Equation 33 contains complex wave numbers of dissimilar modes and further general evaluation may be inexpedient. However, a number of special but important cases can be investigated to derive helpful guidelines for the test-rig design. In case of coupling of similar modes, but in up- and downstream direction, Equation 33 simplifies with $m_{i_1} = m_{i_2} = m_i$. Substituting the wave number from Equation 11 in Equation 33 then gives

$$2\pi f = c\,(1 - M^2) \sqrt{\left(\frac{\pi l}{z_{j_2} - z_{j_1}} \right)^2 + \frac{\kappa_{i_1}^2}{(1 - M^2)}} \quad , \tag{34}$$

where $2\pi f = \omega$ is the frequency in 1/s.

Equation 34 gives singular frequencies around which there will be an increased measurement uncertainty. This will be referred to as 'weak singularities' corresponding to spatial sampling along the duct axis that corresponds to the periodicity of pressure maxima/minima. For plane wave sound propagation in a circular duct, Equation 34 simplifies to (with l=1)

$$\begin{aligned} z_{j_2} - z_{j_1} = & \quad 0.5\frac{c}{f}(1-M^2) \\ = & \quad \tfrac{1}{2}\lambda(1-M^2), \end{aligned} \tag{35}$$

where λ is the wave length of the sound wave. Equation 35 corresponds to the well-known condition for microphone separation for the two-microphone method [16].

Another special case of weak singularities occurs for frequencies where $k_{+i} = k_{-i}$, which is for the cut-on frequency of the corresponding mode ($k_i(f_{cuton}) \to 0$). From Equation 33 follows, that the cut-on frequencies must be singular, regardless of the sensor positions.

We can further derive a formulation for couplings between contra-wise spinning azimuthal modes directly from Equation 33, if we set $m_{i_1} = -m_{i_2} = m_i$ and $k_{i_1} = k_{i_2}$

$$(\phi_{j_1} - \phi_{j_2}) = \frac{\pi l}{m_i} \quad , \quad m_i \neq 0 \quad . \tag{36}$$

Equation 36 may be interpreted as an application of the Nyquist criterion for azimuthal mode capturing. Since it is not a function of frequency, couplings of azimuthal mode pairs occur with their cut-on frequency and remain for all frequencies above. We refer to the arising singularity as a 'strong singularity' that is defined by the angular separation of azimuthal pressure maxima/minima.Another interpretation of Equation 33 follows from the circumstance that $k_{i_1} \approx k_{i_2}$ for $f \gg \kappa_{i_{1/2}} c$. It follows, that pure radial modes ($m = 0$) necessarily couple for high frequencies if they are measured with wall mounted microphones.

Equation 34 and 36 constitute appropriate guidelines to decide sensor positions that lead to well-conditioned system matrices. The condition number of $\mathbf{M}$ improves if we create setups which fulfil those conditions for as many sensor pairs as possible. However, mode coupling for more than two modes may appear in advanced setups with numerous sensors. Predicting this demands solutions for higher order versions of Equation 26, whereas an analytical solution might not be evaluable. A convenient method to illustrate the strength of a certain sensor configuration and to unmask possible singularities is to calculate the condition number of the modal matrix $\mathbf{M}$ as a function of frequency. A suitable sensor setup results in low condition numbers over the whole frequency range of interest and only comprises weak singularities around the cut-on frequencies.

4.2 Conditions for Non-singular Source Spacing

In Section 3.1, the scattering matrix $\mathbf{S}$ was extracted from a number of decomposed measurements under external acoustic excitations. This step also involves a matrix inversion, i.e. of the external pressure matrix $\mathbf{p}_-$ (Equation 13) with the different pressure fields as columns. The condition of this inversion is constituted by the positions of the sources.

We assume a set of perfect monopole point sources and their positions are written as a vector, corresponding to Equation 4

$$\boldsymbol{\Upsilon}_s = [(\Phi_0, z_0, r_0, q_0), (\Phi_1, z_1, r_1, q_1), \ldots, (\Phi_k, z_k, r_k, q_k)]\,, \tag{37}$$

where Υ_{s_j} contains the cylindrical coordinates (Φ_j, z_j, r_j) and the volume velocity q_j in the frequency domain of the j-th point-source position and the number of sources is k. Assuming reflection free duct terminations and

following the formulation of Goldstein [25], we can describe the pressure field excited by a perfect monopole source Υ_{s_j} using the notation from Equation 7 as

$$\begin{aligned} p_j &= q_j \frac{c\rho}{2} \sum_{i=1}^{N} \alpha_i C_{j,i} exp(\mathbf{i}(m_i(\phi_j) + k_i(x_j)) \\ &= q_j \frac{c\rho}{2} \sum_{i=1}^{N} \alpha_i \Psi^*_{j,i} T^*_{j,i} \quad , \end{aligned} \tag{38}$$

with $\alpha_i = 1/\sqrt{1-(\kappa_i c/\omega)^2(1-M^2)}$ and * denotes the operator for the complex conjugated. We define a matrix $\mathbf{G}_\pm$ which describes the monopole fields of the sources

$$p_{i,j} = G_{i,j}\tilde{q}_j \quad with \quad G_{i,j} = \alpha_i \Psi^*_{j,i} T^*_{j,i} \quad , \quad \tilde{q}_j = q_j \frac{c\rho}{2} \quad . \tag{39}$$

We can write Equation 39 in matrix notation for excitations at the upstream and downstream side of the multi-port

$$\mathbf{p}_+ = \mathbf{G}_+ \mathbf{q} \tag{40}$$

$$\mathbf{p}_- = \mathbf{G}_- \mathbf{q} \quad . \tag{41}$$

The condition that we sufficiently excite all modes in the $\pm$ direction corresponds to that $\mathbf{G}_\pm$ is non-singular. Comparing Equation 39 and Equation 9 shows that $\mathbf{G}_\pm$ and $\mathbf{M}_\pm$ have a similar structure and we can derive the same conditions for non-singularity as in Section 4.1 also for $\mathbf{G}_\pm$.

One has to note, however, that the source matrix $\mathbf{G}_\pm$ and the decomposition matrix $\mathbf{M}_\pm$ mathematically have the same structure, but they usually do not have the same number of rows as the number of sources and the number of sensors of a test setup may be different. We can then not conclude an appropriate source-spacing from existing optimised sensor spacings and vice-versa as a submatrix of $\mathbf{M}_\pm$ and $\mathbf{G}_\pm$ does not necessarily have to be well-conditioned. The conditions in Section 4.1 must be applied to sensor and source spacing in separate steps followed by two (separate) optimisations as described in Section 5.1.

In the design for the source section, we have to account for the bulkiness of common loud-speaker sources which increases their minimal possible distance and decreases the upper limit of resolvable frequencies. The derivation in this section is, furthermore, only valid for source arrays in infinite ducts i.e., with low internal reflections as Equation 38 uses the free field greens function. In real ducts, however, the excitation can be disturbed, i.e. if the sound sources are in pressure nodes due to reflections at the duct terminations or the test object. An over-determination within the source array reduces both of these problems and ensures that all modes are excited for the frequencies of interest. Improved results using over-determination were shown in previous work by Holmberg et al. [3]. However, the internal reflections of the test-rig depend on the test-object and the specific boundary conditions and are usually not known during the test-rig design. In order to detect disturbed data, the condition number of $\mathbf{p}_-$ should be computed during measurements/computations for each frequency of interest. In case of numerical computations, single modes can be created separately prescribing source distributions over a cross-section (Section 3.2) which makes $\mathbf{p}_-$ diagonal and hence well-conditioned. The problem of pressure nodes due to internal reflections, however, remains.

4.3 Optimisation of the Sensor Positions

Equation 34 and 36 already provide necessary conditions for non-singular sensor spacing. However, the invertability of the modal decomposition matrix still varies with the sensor spacing, even if both conditions are formally fulfilled. We can evaluate the quality of a certain sensor configuration by computing the condition number of the modal matrix $\mathbf{M}$ over the frequency range of interest. We show how to use the condition number in order to optimise a given sensor array. As an optimisation strategy, we apply a genetic algorithm (GA). Due to their short convergence-time even for multi-dimensional equations, GA find broad application in engineering optimisation, e.g. in [26–28]. A genetic optimisation consists of three steps, as shown in Figure 4. First, a number of initial sensor arrays are computed by randomly change (mutate) the sensor positions of an initial setup. Such an initial setup can for instance be a non-singular setup which was created with condition 34 and 36. The set of all mutated sensor arrays is referred to as a population and each single sensor array is a candidate solution of this population. Second, based on a frequency averaged condition number, the quality of each candidate solution is evaluated and the candidates with most promising condition numbers are chosen to create a new set of enhanced candidate solutions. In a third step, we recombine and mutate those candidates to span a new generation of candidate solutions. We repeat step two and three until we reach convergence and the optimisation of a population is finished [29]. To decrease the chance of detecting local minima, we repeat the optimization with several start-populations until we reach converged optimised condition numbers.

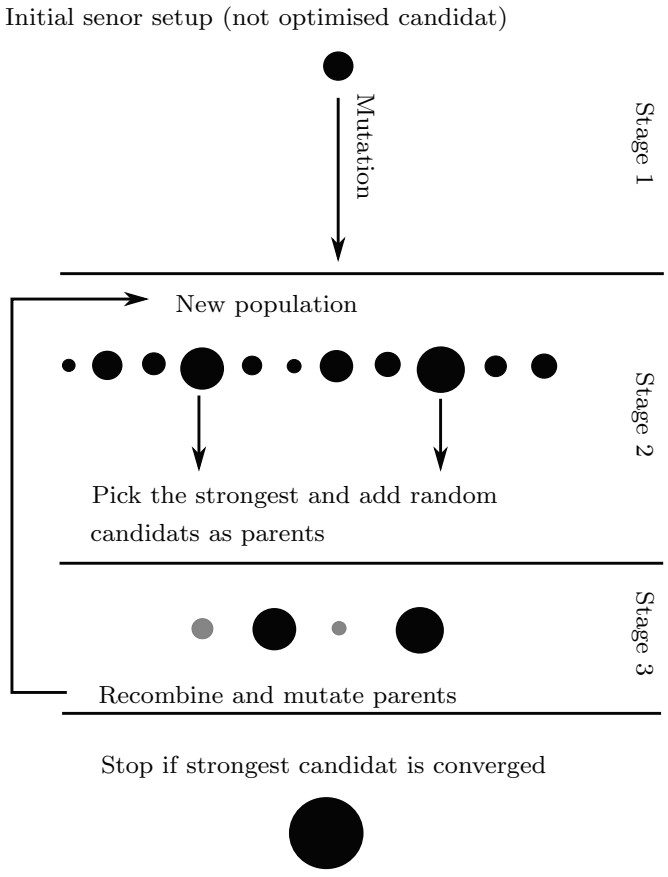

Figure 4: A schematic diagram of the Genetic Algorithm used.

5.0 QUALITY EVALUATION OF MULTI-PORT DATA

Quality evaluation of multi-port data for higher order acoustic modes had very little attention in the literature. Åbom and Bòden [15] gave complete uncertainty analysis for the two-microphone method amongst others including uncertainties due to turbulent flow noise, incorrect wave number estimates, inaccurate microphone positions, and imperfect microphone calibration. Peerling [30] extended this work to describe the uncertainties in the scattering of an acoustic two-port. However, both investigations are based on multivariate uncertainty analysis, which demands the partial derivatives of all uncertain parameters. The complexity of that approach increases significantly with the number of sensors. It, furthermore, only accounts for linear uncertainty propagation, which is not necessarily given for wave-decomposition and scattering computation in over-determined sensor and source arrays. Schultz et al. [18] applied a Monte-Carlo method to two-port data to account for non-linear uncertainties. We extend this work and apply a Monte-Carlo method to the scattering matrix calculation of a higher order acoustic multi-port and account for uncertainties due to noise in the pressure-signals and due to errors in the wave number estimate. The measurement noise is, therefore, estimated using the coherence between the sensors and sources, see Section 5.1. To estimate the uncertainties in the flow-velocity and the temperature, we use the full wave decomposition, see Section 5.2.

5.1 Error Estimation with the Monte-Carlo-Method

A schematic diagram of the Monte-Carlo Method used can be seen in Figure 5, which follows the suggestions in Ref. [31].

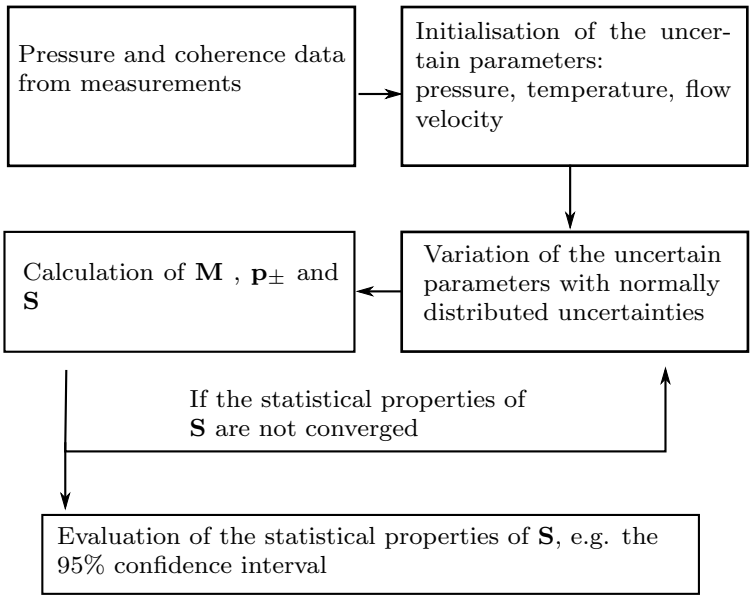

Figure 5: Schematic diagram of the MCM used.

The pressure signals of the sensors, the temperature and the flow-velocity are treated as statistical properties with standard distributed noise around the measured mean value. We decompose the measured sound fields for each set of those distributions and compute the scattering matrix. The statistical variations of its components from all computed sets are used to compute the 95 % confidence interval of the results. However, we need to

estimate the uncertainties in the input variables, i.e. the uncertainty induced by the sensor signal noise and the flow properties.

The relative uncertainties ϵ_r in the pressure-signals can be computed following Bendat and Piersol [32]. We concentrate on the system noise which was addressed as a dominant contributor to the random uncertainties of two-port measurements by Peerlings [30]. It contains all the normal-distributed noise of the reference signal and the final data, e.g. flow-noise, amplifier-noise, acquisition noise. We use the coherence γ in order to estimate the spectrum of the random noise in our measurements

$$\mathrm{G_{nn}} = (1-\gamma^2_{\mathrm{xy}})\mathrm{G_{yy}},\ \gamma^2_{\mathrm{xy}} = \frac{|\mathrm{G_{xy}}|^2}{\mathrm{G_{yy}G_{xx}}},\ \mathrm{H_{xy}} = \frac{\mathrm{G_{xy}}}{\mathrm{G_{xx}}}, \tag{42}$$

where $\mathrm{G_{yy}}$, $\mathrm{G_{xx}}$ and $\mathrm{G_{nn}}$ are the estimates for the auto-spectra of the input, the output and the noise, respectively. The function G_{xy} is the cross-spectrum and H_{xy} is the H_1-transfer function between the reference and the source signal. If we assume a normally distributed measurement noise, we can express its absolute error as

$$\begin{aligned} \epsilon_a(G_{nn}) = &\ \frac{G_{nn}}{\sqrt{n_d}} = \frac{(1-\gamma^2_{xy})|G_{xy}|^2}{G_{xx}\gamma^2_{xy}\sqrt{n_d}} \\ = &\ \frac{(1-\gamma^2_{xy})|H_{xy}|^2 G_{xx}}{\gamma^2_{xy}\sqrt{n_d}} \quad . \end{aligned} \tag{43}$$

For the Monte Carlo computation we derive the relative error contributed by the system noise normalised to the cross-spectra $|\mathrm{G_{xy}}|$

$$\epsilon_{\mathrm{r}}(\mathrm{G_{nn}}) = \frac{(1-\gamma^2_{\mathrm{xy}})|\mathrm{H_{xy}}|}{\gamma^2_{\mathrm{xy}}\sqrt{\mathrm{n_d}}} \quad . \tag{44}$$

5.2 Estimation of Temperature and Mean-Flow Velocity

In measurement setups for higher-order multi-port eduction, the decomposition matrix is overdetermined with sensor points in the plane wave region which enables us to solve the linear system in Equation 8 for additional unknowns. Allam and Åbom [33] proposed the full wave decomposition method in order to estimate the wave number from overdetermined plane wave measurements. This method applies an iterative optimisation algorithm to an initial guess of the wave number obtained from temperature and velocity measurements of the flow field in order to solve for the wave number. Holmberg et al. [3] deployed the method for accurate two-port measurements and reported an improvement, although they only concentrate on the real part of the wave number. The values obtained with that method vary over frequency and Holmberg proposes to use an average Mach-number value.

Instead of using an iterative optimisation algorithm to fit for the wave number, we estimate the flow velocity and temperature from the error in the over-determined decomposition. Therefore, we use one of the wave number estimators from Section 2.2. Here, we apply the wave number in Equation 11 but the method is not restricted to that estimator. We define a vector $\mathbf{p_d}$ of complex modal-amplitudes that results from a modal decomposition of a pressure field $\mathbf{p_m}$

$$\mathbf{p_d} = \mathbf{M}^{-1}\mathbf{p_m} \quad . \tag{45}$$

The decomposition matrix $\mathbf{M}$ contains exponential functions of the uncertain wave number and hence propagates its uncertainties into $\mathbf{p_d}$. If $\mathbf{M}$ is over-determined, the Moore-Penrose-Pseudo inverse solves Equation 45, using a least-error method. If we now re-compose the sound field

$$\mathbf{M}\mathbf{p_d} = \tilde{\mathbf{p}}_\mathbf{m} \quad , \tag{46}$$

we obtain the pressure field $\tilde{\mathbf{p}}_\mathbf{m}$ where $\tilde{\mathbf{p}}_\mathbf{m} = \mathbf{p}_\mathbf{m}$ only for square decomposition matrices. For overdetermined decomposition matrices, $\tilde{\mathbf{p}}_\mathbf{m}$ differs from $\mathbf{p}_\mathbf{m}$, and the difference between those two vectors is larger with increasing uncertainties in $\mathbf{M}$. We can state a value for an averaged error E

$$\mathrm{E} = ||\mathbf{M}\,\mathbf{p}_\mathbf{d} - \mathbf{p}_\mathbf{m}|| \quad , \tag{47}$$

where $||\ldots||$ is the euclidean norm. Equation 47 can be used to estimate the wave number, eg. by computing E over a grid of velocity and temperature values. The minimum value of E corresponds to the wave number that allows the best decomposition, i.e. the best agreement of the measured fields to the analytic solution. If we compute the wave number for a number of low frequency measurements, we can compute the mean values of the flow-parameters and their standard deviation that we use as uncertainty parameters for the Monte-Carlo simulation.

6.0 RESULTS

To apply our theory, both experiments and computations were performed. The purpose of these tests was as follows:

1. To show the necessary steps in the test-rig design in order to create sensor arrays with well-conditioned decomposition matrices (Section 6.1). We compared the theoretical uncertainty propagation through a complete scattering computation of the test cases A) a highly overdetermined, but non-optimised setup and B) a not overdetermined but optimised setup, using the theory from Section 4.0.

2. To gain measurement results of an optimised test-rig for multi-ports of the order 6. We applied the theory from Section 2.0 to decompose the measured sound fields and to compare the three different wave number estimators. As a test case, we chose the empty duct with low Mach-number flow (M=0.1), as this case is well-studied [34] and the analytical solution is pure transmission without reflection. We used the coherence to estimate the signal noise (Section 5.1) and the full wave decomposition (Section 5.2) to solve for the flow properties in order to compute the error bars with the Monte-Carlo Method.

3. To apply the decomposition to numerical data and to compare the results with measurements. We computed the scattering of a circular orifice plate without mean flow, using the theory from Section 3.2. In Ref. [6] it was shown, that the demonstrated method works well for cases with mean-flow in the plane wave range. One can argue, that the results in Ref. [6] can also be accomplished for higher order modes in the same way, as the equations are linear and the modes are eigen-solutions of those equations. Adding turbulent flow would, however, increase random uncertainties in the data and may introduce bias errors into the wave-numbers and mode-shapes due to non-uniform flow profiles, see Ref. [35].

6.1 Test-rig Design

The experiments presented are tests done as part of the work within the framework of the European Project 'IdealVent' (Integrated Design of Optimal Ventilation Systems for Low Cabin and Ramp Noise). The goal of this project was to characterise components of an air-conditioner system as it can be found in common aircraft, using aeroacoustic multi-ports. The data was gained with different measurement setups and numerical approaches and compared to validate and evaluate the established methods and models. In order to take comparable data, a number of agreements about the conditions in measurement and computation had to be defined, which are presented in Table 1.

Table 1: Conditions for the test-rig design

Frequencies	500 Hz - 3000 Hz
Flow velocity	30 m/s
Duct, diameter	circular, 0.15 m
Temperature	(288 - 298) K

Based on these conditions, the cut-on frequencies of interest were computed with the roots of the imaginary part of the convective wave number in Equation 11

$$\sqrt{1-(\kappa_{mn}c/\omega)^2(1-M^2)}=0 \tag{48}$$

to be $f_{10} = 1337\,\mathrm{Hz}$, $f_{20} = 2217\,\mathrm{Hz}$, and $f_{01} = 2780\,\mathrm{Hz}$ for $c = 343\,{}^{m}/_{\mathrm{s}}$ which results in a total number of six propagating modes. Following Section 2.0, we need at least 12 sensor points upstream and downstream in order to decompose the sound fields into the modal components and at least six external sources upstream and downstream to compute the full scattering matrix. We compared two setups: A) non-optimised and B) optimised. In A), we applied 16 sensors and 12 sound sources upstream and downstream in a simple, unoptimised setup to achieve a measurement with over-determination in sources and sensors. This setup was only investigated theoretically. In B), we used a minimum of 12 Brül and Kjaer ¼-inch 4938-A11 high pressure microphones upstream and downstream and a slightly over-determined source array with 8 sources in an optimised assembly. As a guide line for both setups, we apply the conditions 34 and 36. Equation 34 was used to solve for the axial sensor separation. It is clear, that κ_m in Equation 34 and hence also the singular frequency increases with the mode order, which reduces the maximal possible axial separation of sensors to the plane wave condition in Equation 35 in our case to $\Delta z < 48\,\mathrm{mm}$. For the azimuthal sensor positions we satisfied condition 36 for $m = 1, 2$ for at least two microphones per mode. For case A), we divided the sensor array in four cross-sections with four sensors each and broke the occurring symmetry for the (2,0)-mode at two sensor positions (Sensor 9 and 16). A more detailed description of this design can be found in Ref. [12], where the sensor array in Table 2 is adopted. The flow speed and the flow velocity for the wave number estimates were measured with a pitot-tube upstream of the test section (flow velocity) and a thermo-couple down stream of the test section (temperature) and additionally fitted with the full wave decomposition (Section 6.7)

Table 2: Sensor positions of test A). Mic.:number of sensor, Pos.:axial position in mm, Ang.:azimuthal position in deg

Mic.	Pos.	Ang.	Mic.	Pos.	Ang.	Mic.	Pos.	Ang.	Mic.	Pos.	Ang.
1	0	0	**5**	40	0	**9**	110	0	**13**	150	90
2	0	90	**6**	40	90	**10**	110	90	**14**	150	180
3	0	180	**7**	40	180	**11**	110	180	**15**	150	270
4	0	270	**8**	40	270	**12**	110	225	**16**	150	315

6.2 Optimization of the Sensor Positions

Test case B) originated from the genetic optimisation described in Section 4.3. We used a frequency averaged condition number of the decomposition matrix $\mathbf{M}$ as the criteria for the optimisation. We computed the condition number for 105 frequencies and weighted their average for higher frequencies to especially focus on the

accuracy of the higher order acoustic-modes. However, one can also consider weight-functions, which focus on frequency bands of particular interest, e.g. the harmonics of a fluid-machine.

We started the optimisation with a random distribution of 12 sensor points which fulfilled the conditions for none singular wave decomposition and optimised over 3600 generations. Figure 6 a) shows the averaged condition number over the generations during the optimisation. Sudden jumps in the graph indicate iterations where the optimisation has converged and a restart was prescribed. The GA decreased the mean-condition number to 2.3, whereas the mean condition number with the same weighting of test case A) was 5.9. Single populations converged already after less than 40 generations (Figure 6 b). Even after the 30 first iterations, the initial condition number has been reduced by more than 50 percent to 2.6. The minima that we found for each population are local. A higher number of computed populations enhanced the condition number further but the enhancement from the highest converged optimisation to the lowest was only 12 percent from 2.6 to 2.3.

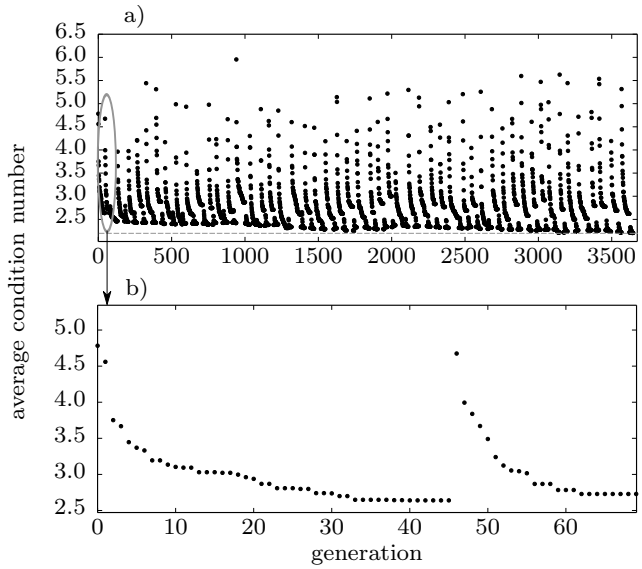

Figure 6: a) Data for the optimisation with a GA for 3600 generations. The mean-condition number shows several local minima. Dashed line: optimised condition number b) the convergence of the first population. A strong gradient and convergence after 35 generations.

The optimised sensor section is presented in Table 3. The optimised axial positions showed a wider distribution than the none-optimised setup in Table 2 which is in accordance with Equation 30 where a higher number of axial position reduces the coupling within the radial modes. The optimised azimuthal positions renounced angles fulfilling condition 36, which resulted in more stability in the azimuthal mode separation. Both effects were visible in the condition number of the optimised configuration (Figure 7). Even if we indicated a slight decline in the plane wave range, the calculation showed a significant improvement after the cut-on of the ($\pm$2,0)-mode

Table 3: Sensor positions for the optimised setup B). Mic.:number of microphone, Pos.:axial position in mm, Ang.:azimuthal position in deg

Mic.	Pos.	Ang.	Mic.	Pos.	Ang.	Mic.	Pos.	Ang.	Mic.	Pos.	Ang.
1	0	0	**4**	60	125	**7**	100	70	**10**	140	315
2	40	265	**5**	70	205	**8**	100	145	**11**	140	80
3	50	20	**6**	90	295	**9**	120	205	**12**	180	345

and (0,1)-mode. For these regions, we reduced the condition number by up to a factor of 3.

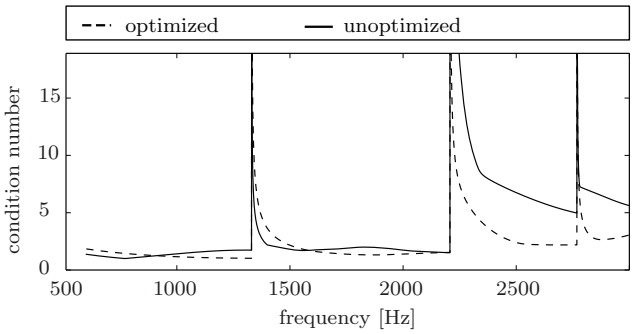

Figure 7: Condition number of the unoptimised, but over-determined A) (solid line) and the optimised B) (dashed line) sensor array

6.3 Theoretical Uncertainty Propagation

We investigated the uncertainty propagation applying the Monte Carlo Method to both setups for computed pressure fields. The pressure fields were computed using the source positions from Ref. [12] for test-case A) and an optimised source section for test-case B).

First, we performed a convergence study at 2900 Hz for test-case A) on the unoptimised sensor arrays for the (1,0)-mode. We assumed that the MCM converges slowest for the lowest over-determination and the highest mode. We computed the uncertainties for a large number of test-samples. The Monte Carlo simulation approached convergence between 200000 and 400000 samples. We used 400000 samples to compute the theoretical uncertainty propagation through test-cases A) and B) (Figure 8). An uncertainty of 2 % in the smooth estimate of the pressure values was assumed. Case A) (white markers) showed small uncertainties for low frequencies, but strongly increased uncertainties especially after the cut-on frequency of the (2,0)- mode. The strong coupling in most of the sensor points for the (2,0)-mode affected this mode particularly. The optimised setup in case B) (black markers) accounted for that problem and reduced the uncertainties in the (2,0)-mode by a factor higher than 2. As a result of the optimisation, we could find a more uniform propagation of uncertainties to the single modes, which all showed very close uncertainty values.

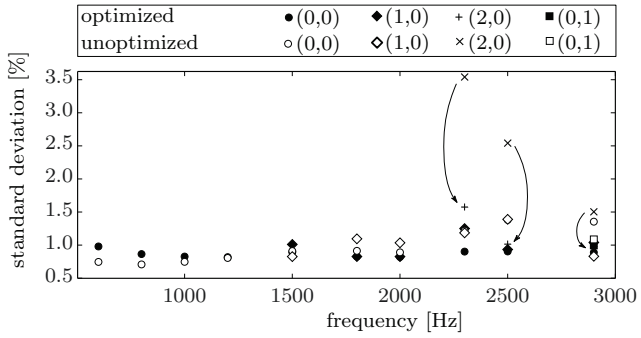

Figure 8: Comparison of the uncertainty propagation between the unoptimised setup A) (white markers) and the optimised setup (black markers) B).

6.4 Remark on the Effect of Over-determination

Table 4: Mean condition number of the modal matrix for optimised sensor arrays. Mic.:number of sensors in the array. Cond.:averaged condition number of M

Mic.	cond.	**Mic.**	cond.	**Mic.**	cond.	**Mic.**	cond.	**Mic.**	cond.
12	2.388	**13**	2.147	**14**	1.942	**15**	1.921	**16**	1.809

Holmberg et al. recognised a positive effect on the stability and accuracy of the scattering computation using over-determined sensor and source arrays [3]. However, the effect of over-determination is not mainly induced by the number of additional sensors but by their actual position relative to a reference sensor and is hence always related to certain sensor spacing. With the optimisation strategy presented in Section 4.3 we can design sensor arrays with enhanced condition numbers. The optimal condition number is unique for the number of used sensors and can be compared which gives a reasonable measure for the effect of over-determination. We applied the genetic algorithm to sensor arrays containing an increasing number of sensor points. As a result, the mean condition number of the modal matrix for the optimised sensor arrays can be seen in Table 4. It was found that the condition number decreased with a higher over-determination for optimised sensor arrays. Figure 9 shows the condition number as a function of frequency and number of optimised sensors. Due to the weighting for higher frequencies in the computation of the mean condition number in our optimisation, the over-determination mainly influenced the higher order modes. The gain for additional over-determination was much stronger for a low number of sensors. The effect of two additional sensors from 12 to 14 decreased the condition number by around 20% at 2900 Hz, whereas we saw only 7% improvement between 14 and 16 sensors for the same frequency.

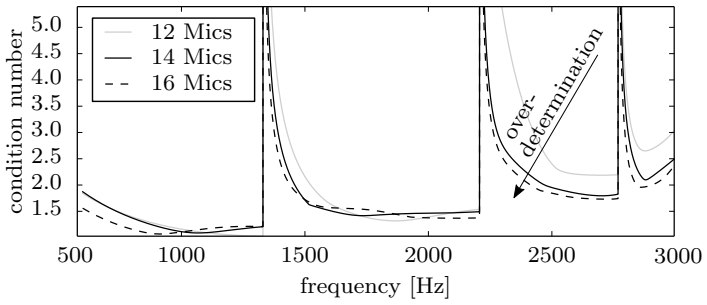

Figure 9: Condition number as a function of frequency. Effect of over-determination in the sensor array on the over-all condition number. Computed for optimised sensor positions.

6.5 Scattering of the Empty Duct

We used the optimised test-setup (case B)) from Section 6.2 to measure the full scattering of the empty duct ($R = 150\,\mathrm{mm}$) with mean flow ($v = 30\,{}^{m}\!/\!_{\mathrm{s}}$) for 100 frequencies from 500 Hz to 3000 Hz. The empty duct element was $1100\,\mathrm{mm}$ long, measured from the closest microphones on the upstream and downstream side. The microphones were calibrated for phase and amplitude for all frequency points following the procedure used in [16]. The source sections were placed upstream and downstream, behind the sensor section. To reduce possible structural vibrations, the duct of the source sections was not physically connected to the test sections, following the advices in Ref. [30]. The gaps in the channel wall between the source part and measuring part

of the test-rig were closed with tape. The velocity was measured with a Pitot-tube far upstream of the test object to ensure undisturbed inflow and we measured the center-line velocity. The temperature was measured with a thermocouple inside the duct wall downstream of the test-object. The duct was made of 5 mm thick aluminium. The inlet was connected to a pressurised chamber and the outlet to a muffler. A schematic sketch of the measurement assembly can be seen in Figure 10.

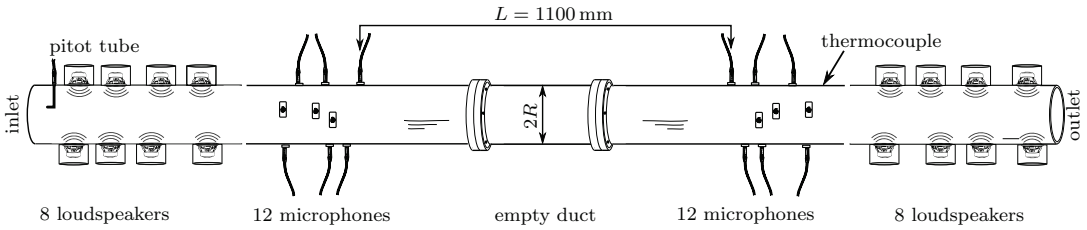

Figure 10: Schematic sketch of the measurement assembly.

We measured the cross-spectra between the sources and the sensors for a simultaneous sinusoidal excitation of six sources at uncorrelated frequencies and decomposed the sound fields into their modal components using the theory from Section 2.0. Figure 11 shows the measured magnitude of the transmission coefficient ($|\mathbf{S}_{i,i+6}|$) and reflection coefficient ($|\mathbf{S}_{i,i}|$) of the empty duct for all the six propagating modes upstream and downstream. The analytical solution is pure transmission ($|\mathbf{S}_{i,i+6}| = 1$) and no reflection (($|\mathbf{S}_{i,i}| = 0$)). We measured values which were very close to the analytical solution. The (0,0)-mode differed less then 2%, the (1,0)-mode and (0,1) less than 3%, and the (2,0)-mode less than 5% as an negative offset from the analytical solution, where we used Dokumaci's wave number estimator for the post-processing. A comparison to the other estimators is made in Section 6.6.

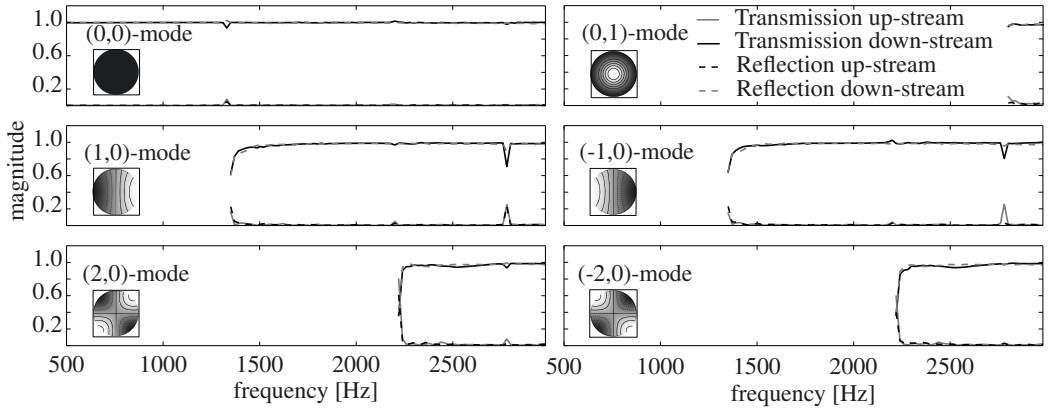

Figure 11: The magnitude of the transmission and reflection coefficients of the empty duct upstream and downstream.

The only larger disturbances we noticed were at the cut-on frequencies where we received spikes in the scattering computation. This behaviour corresponds to the investigations in Section 4.1 as the decomposition becomes singular for those frequencies. Another disturbance we noticed was a transmission drop of around 5% for the ($\pm$1,0) and ($\pm$2,0)-mode close to their cut-on frequencies. Tests with additional weights that we applied to the shell of the duct element indicated a coincidental resonance in the channel walls at those frequencies. This effect is discussed in detail, e.g. in Ref. [36].

6.6 Comparison of Different Wave Number Estimators

We computed the scattering of the empty duct for the three different wave number estimators discussed in Section 2.2. To make the results comparable, we post-processed the same data using the same velocity, temperature and duct-length. Figure 12 shows the magnitude of the transmission coefficients of the empty duct at the upstream side ($|\mathbf{S}_{i,i+6}|$) calculated with the different dissipation models. Dokumaci's model showed the results which where closest to the analytical solution. Since the wave number solution of Dokumatci equals the Kirchhoff solution for the (0,0)-mode, there was no difference between both for the (0,0)-mode. The improvement for higher order modes, however, is remarkable. The Kirchhoff wave number enhances the solution of the transmission coefficient for the higher order modes by around 3 % whereas we found the wave number with Documaci's approach to be increased by more than 5 %. The shape of curves, however, was not affected by the used model.

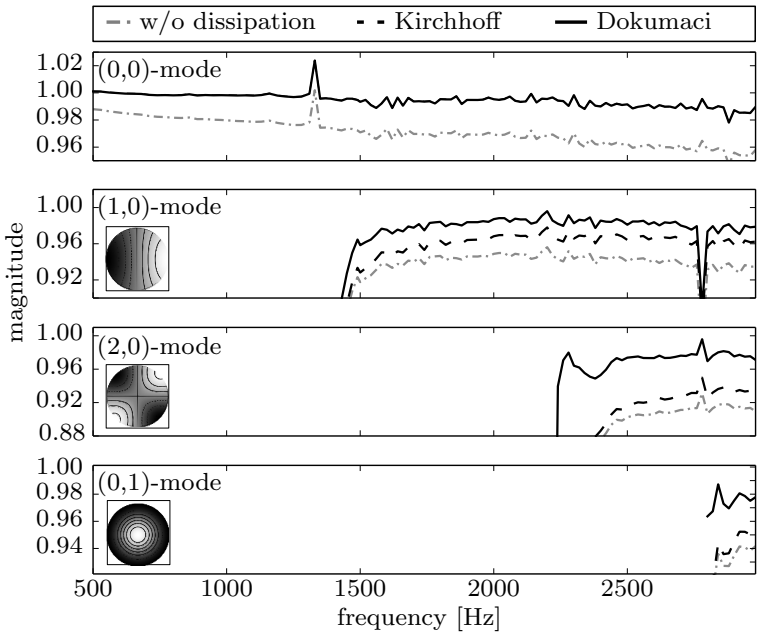

Figure 12: Comparison of Dokumaci's [21] (solid line), Kirchhoff's (dashed line) and a non-dissipative (dashed-dotted line) wave number model for transmission calculation of an empty duct (Length = 1100 mm and v=30 m/s) from upstream to downstream direction.

6.7 Uncertainty Estimation for the Empty Duct Measurements

We estimated the uncertainties due to noise in the pressure signals and uncertain flow properties. We computed the coherence from the measured auto-spectra and cross-spectra (Equation 43) for each sensor and used this information to estimate its standard deviation due to signal-noise (Equation 44).

To estimate the uncertainty in the flow parameters, we used the full wave decomposition from Section 5.2 on the plane wave range of our measurement. We computed the flow velocity and the temperature for 27 frequencies and used the mean value as a guess for the measurement properties, as proposed in Ref. [3]. The standard deviation of those values was the input for the Monte Carlo simulation. Figure 13 shows an excerpt of the data for two flow velocities (0 m/s (a),(b) and 30 m/s (c),(d)) for two different frequencies (500 Hz (a),(c)

Table 5: Results from the wave number fitting. v in [m/s] and T in [K]

a)	T measured	T fitted	b)	v measured	v fitted
500 Hz, 0 m/s	294.45	295.35	**500 Hz, 0 m/s**	0.0	-0.20
500 Hz, 30 m/s	292.55	295.36	**500 Hz, 30 m/s**	30.0	27.76
1100 Hz, 0 m/s	294.45	294.95	**1100 Hz, 0 m/s**	0.0	-0.20
1100 Hz, 30 m/s	292.55	293.56	**1100 Hz, 30 m/s**	30.0	28.98

and 1100 Hz (b),(d)). The plots show the grid of velocity and temperature on which we solved Equation 47. The shades show the averaged error which we normalised to the averaged error of our initial guess ($T = 293\,\mathrm{K}, v = 0\,{}^{m}/_{\mathrm{s}}$ for a) and b) and $v = 30\,{}^{m}/_{\mathrm{s}}$ for c) and d)). The contour-lines can be interpreted as lines of constant error, i.e. lines of constant wave numbers. We found, that the flow velocity has only little influence on the density of the contour lines and hence on the susceptibility to uncertainties. However, the frequency had a large impact on the error in the decomposition. As the wave number in plane wave range is a linear function of the frequency, this behaviour was reasonable.

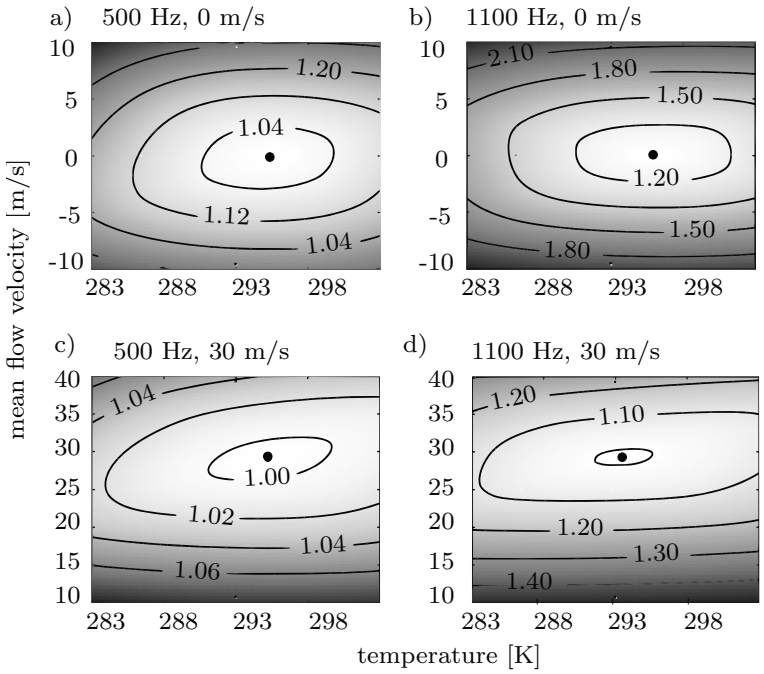

Figure 13: Temperature and velocity estimation based on Section 5.2. The shades show the normalised, averaged error (Equation 47). The contour lines are circles of constant wave number.

In Table 5 we show the results from the wave number fit averaged over 27 frequencies compared with results obtained from the thermocouple and pitot tube. The obtained values for the temperature were stable and differed less than one percent from the measured values (Table 5 a)). The standard deviation of the temperature and velocity for all of the 27 frequencies were low $(293.00 \pm 0.33)\,\mathrm{K}$ and $(28.92 \pm 0.18)\,\mathrm{m/s}$.

We used the estimated noise and the standard deviation of the flow properties to perform a MCM on the measurement data and computed the error-bounds presented in Figure 14. The grey areas show the 65% and 95% confidence interval of the scattering data. We found, that the uncertainty increases with the number of

propagating modes which was due to the decreasing over-determination in the sources and sensors. The error bounds did not result in a smooth curve but in spikes for certain frequencies, which coincided with the findings in Ref. [30]. One has to point out that the method only considered some of the uncertainty sources and only random uncertainties. Others, e.g. uncertainties in the microphone-positions, the dimensions of the duct, and structural vibrations introduce additional errors and the given error bars hence underestimated the actual error bounds. We found weaknesses in the method particularly at the cut-on frequency, where the error was highly underestimated.

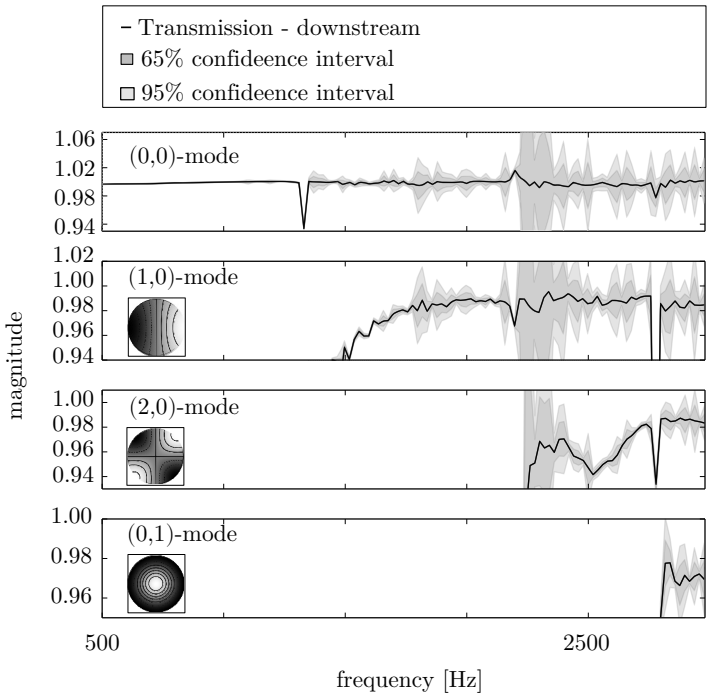

Figure 14: Uncertainty estimation for the empty-duct measurements applying the MCM based on the signal coherence and the uncertainty in the wave number.

6.8 Scattering of an Orifice Plate

To demonstrate the method on numerical data using highly overdetermined decomposition matrices, we computed the scattering of a circular sharp edged orifice plate without flow. The thickness of the plate was 1.6 mm and the aperture had a radius of 56 mm. We solved Equation 22 and Equation 23 with the acoustic solver in COMSOL Multiphysics®. We discretised the orifice and the duct 4 duct diameters upstream and downstream with a total number of 65.000 hexahedral elements in an axial and circular structured three dimensional grid. The terminations of the duct were modelled with perfectly matched layers in order to decrease reflections [6]. We increased the mesh density close to the orifice as we expected the presence of evanescent modes in the acoustic near field. We applied the modal decomposition to the pressure data that we sampled at all the grid points on both sides of the orifice in a distance of at least one duct diameter to exclude the acoustic near field from the modal decomposition. We computed the scattering at 55 frequency points for all propagating modes. The results can be seen in Figure 15 in comparison to measurements taken on a similar orifice using the method

and the setup from Section 6.5. The results from the computation were completely symmetric for both the upstream and downstream side, and for the +/– modes, so that we only present a part of the magnitudes of the transmission ($|\mathbf{S}_{i,i+6}|$) and reflection coefficients ($|\mathbf{S}_{i,i}|$).

We found, that the mode decomposition with highly overdetermined matrices is well suited to extract scattering data from computations in the frequency domain. We found a very good agreement between the measurements and the computations even for higher order modes. We were able to reproduce both, shape and level of the scattering parameters. Only close to the cut-ons between 1400 Hz and 1500 Hz for the (1,0)-mode, and 2500 Hz and 2600 Hz for the (2,0)-mode, we saw bigger differences, which were due to structural vibrations as pointed out in Section 6.5. We could, furthermore, reproduce the coupling between the (0,0)-mode and the (0,1)-mode, which was visible in the reduced transmission of the (0,0)-mode after the cut-on frequency of the (0,1)-mode.

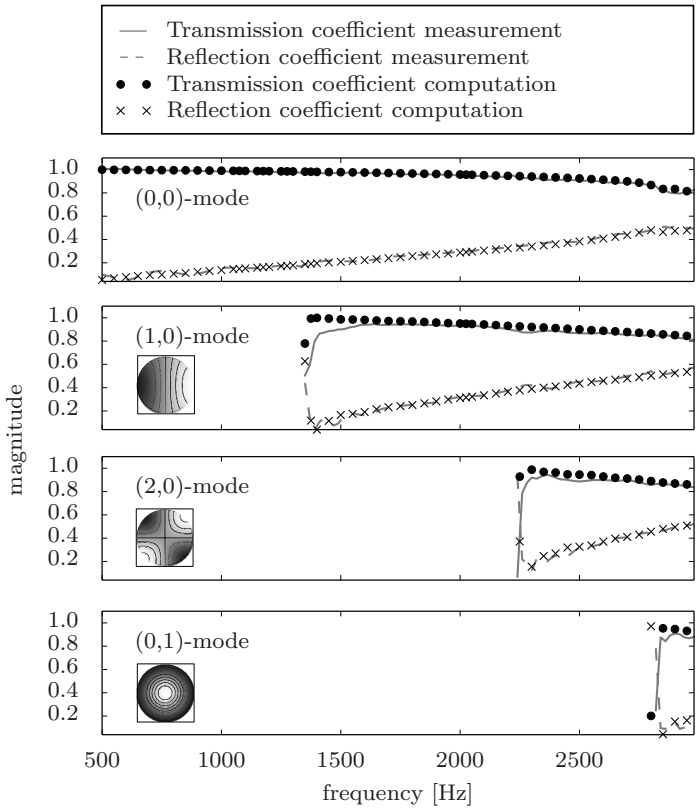

Figure 15: Magnitude of the transmission and reflection coefficients for a circular orifice without flow.

7.0 SUMMARY AND CONCLUSIONS

We presented the theory which is needed to design advanced test-rig setups to determine the scattering of acoustic multi-ports. We showed that the condition number is a strong measure to quickly assess a certain setup and indicate frequencies of singular decomposition. We proposed to follow a number of steps during the test-rig design. First, we proposed the usage sensor positions that avoid weak and strong singularities evoked by mode

coupling of two modes based on analytical solutions. This should be combined with the condition number plot to give a good overview over possible higher order mode coupling. In a second step, we demonstrated how an existing setup can be further optimised. A genetic algorithm applied to the microphone array showed reliable and quickly converging results and enhanced the decomposition especially for higher frequencies. We reduced the mean condition number of the transformed modal matrix by a factor of three (Figure 7). Using optimised setups with different numbers of sensors, we could visualise the positive effect of over-determination. We used calculated sound fields together with our optimised setup in order to perform a Monte-Carlo calculation on the pressure values that showed the positive effects of the optimisation for each of the single modes compared to an unoptimised setup. The uncertainties in the optimised setup moved generally closer together and the strong susceptibility of the (2,0)-mode could be completely removed (Figure 8). To estimate the influence of uncertainties in temperature and velocity, we applied the full wave decomposition. A grid over temperature and velocities showed the minimum average error and furthermore circles of constant wave number, which can be used to estimate the steepness of uncertainty propagation in the wave number. We were able to fit the mean flow velocity and the temperature based on this method. Comparisons with temperature and flow measurements showed a strong agreement with our method. We eventually performed measurements on an empty duct to demonstrate our optimised test setup. We compared three different wave number models, whereas Dokumaci's model gave the best results and enhanced the Kirchhoff model at higher order modes (Figure 12). The determined transmission and reflection was found to be very close to the analytical solution, which indicated a good measurement setup. We finally used the method to measure the acoustic scattering of a circular orifice plate and compared the data to the solution of a numerical computation in frequency domain. By doing so, we demonstrated the high potential of the decomposition method which can be applied to both, measurement and numerical data. We archived very clean data for both cases and showed a remarkable agreement between measurements and computations (Figure 15).

REFERENCES

[1] M. Åbom and H. Bodén, "A note on the aeroacoustic source character of in-duct axial fans," *Journal of Sound and Vibration*, vol. 186, no. 4, pp. 589–598, 1995.

[2] S. Sack and M. Åbom, "Multi-port Eduction for Ducted Components," in *VKI lecture series: Simulation, control and reduction of ventilation noise*, p. 4, 2015.

[3] A. Holmberg, M. Åbom, and H. Bodén, "Accurate experimental two-port analysis of flow generated sound," *Journal of Sound and Vibration*, vol. 330, no. 26, pp. 6336–6354, 2011.

[4] L. D. Santana, W. D. Roeck, and W. Desmet, "Indirect acoustic impedance eduction in presence of flow based on an analytical two-port formulation," *Mechanical Systems and Signal Processing*, vol. 48, no. 1-2, pp. 388–403, 2014.

[5] Y. H. Heo, J. G. Ih, and H. Bodén, "In-duct identification of fluid-borne source with high spatial resolution," *Journal of Sound and Vibration*, vol. 333, no. 23, pp. 6074–6089, 2014.

[6] A. Kierkegaard, S. Allam, G. Efraimsson, and M. Åbom, "Simulations of whistling and the whistling potentiality of an in-duct orifice with linear aeroacoustics," *Journal of Sound and Vibration*, vol. 331, no. 5, pp. 1084–1096, 2012.

[7] A. Holmberg, M. Karlsson, and M. Åbom, "Aeroacoustics of rectangular T-junctions subject to combined grazing and bias flows - An experimental investigation," *Journal of Sound and Vibration*, vol. 340, pp. 1–15, 2014.

[8] J. Lavrentjev and M. Åbom, "Characterization of Fluid Machines As Acoustic Multi-Port Sources," *Journal of Sound and Vibration*, vol. 197, no. 1, pp. 1–16, 1996.

[9] H. Trabelsi, N. Zerbib, J.-M. Ville, and F. Foucart, "Passive and active acoustic properties of a diaphragm at low Mach number. Experimental procedure and numerical simulation," *Revue européenne de mécanique numérique*, vol. 20, no. 1-4, pp. 49–71, 2011.

[10] M. Taktak, J. M. Ville, M. Haddar, G. Gabard, and F. Foucart, "An indirect method for the characterization of locally reacting liners.," *The Journal of the Acoustical Society of America*, vol. 127, pp. 3548–3559, 2010.

[11] T. J. Newman, A. Agarwal, A. P. Dowling, and L. Desvard, "A sound power measurement technique optimised for low-speed fan tones," *International Journal of Aeroacoustics*, vol. 15, pp. 59–80, mar 2016.

[12] S. Sack, M. Åbom, K. Kucukcoskun, and C. Schram, "Generation and scattering of acoustic modes in ducts with flow," in *20th AIAA/CEAS Aeroacoustics Conference*, (Atlanta, USA), 2014.

[13] E. Alenius, M. Åbom, and L. Fuchs, "Large eddy simulations of acoustic-flow interaction at an orifice plate," *Journal of Sound and Vibration*, vol. 345, pp. 162–177, 2015.

[14] J. Lavrentjev, M. Åbom, and H. Bodén, "A measurement method for determining the source data of acoustic two-port sources," 1995.

[15] M. Åbom and H. Bodén, "Error analysis of two-microphone measurements in ducts with flow," *The Journal of the Acoustical Society of America*, vol. 83, no. 6, p. 2429, 1988.

[16] M. Åbom, "Modal decomposition in ducts based on transfer function measurements between microphone pairs," *Journal of Sound and Vibration*, vol. 135, no. 1, pp. 95–114, 1989.

[17] C. H. Gerhold, R. H. Cabell, and M. C. Brown, "Development of an experimental rig for investigation of higher order modes in ducts," *American Institute of Aeronautics and Astronautics*, no. May, pp. 8–10, 2006.

[18] T. Schultz, M. Sheplak, and L. N. Cattafesta, "Uncertainty analysis of the two-microphone method," *Journal of Sound and Vibration*, vol. 304, no. 1-2, pp. 91–109, 2007.

[19] A. Sitel, J.-M. Ville, and F. Foucart, "Multiload procedure to measure the acoustic scattering matrix of a duct discontinuity for higher order mode propagation conditions," *Journal of the Acoustical Society of America*, vol. 120, no. 5, pp. 2478–2490, 2006.

[20] S. Allam and M. Åbom, "Investigation of damping and radiation using full plane wave decomposition in ducts," *Journal of Sound and Vibration*, vol. 292, no. 3-5, pp. 519–534, 2006.

[21] E. Dokumaci, "On the effect of viscosity and thermal conductivity on sound propagation in ducts - A revisit to the classical theory with extensions for higher order modes and presence of mean flow," *Journal of Sound and Vibration*, vol. 333, no. 21, pp. 5583–5599, 2014.

[22] P. O. A. L. Davies, "Practical flow duct acoustics," *Journal of Sound and Vibration*, vol. 124, no. 1, pp. 91–115, 1988.

[23] C. Morfey, "Sound transmission and generation in ducts with flow," *Journal of Sound and Vibration*, vol. 14, no. 1, pp. 37–55, 1971.

[24] R. Lacombe, S. Föller, G. Jasor, W. Polifke, Y. Aurégan, and P. Moussou, "Identification of aero-acoustic scattering matrices from large eddy simulation: Application to whistling orifices in duct," *Journal of Sound and Vibration*, vol. 332, no. 20, pp. 5059–5067, 2013.

[25] M. E. Goldstein, *Aeroacoustics*. 1976.

[26] R. Barbieri and N. Barbieri, "Acoustic horns optimization using finite elements and genetic algorithm," *Applied Acoustics*, vol. 74, pp. 356–363, mar 2013.

[27] J. Zhao and M. Xu, "Fuel economy optimization of an Atkinson cycle engine using genetic algorithm," *Applied Energy*, vol. 105, pp. 335–348, may 2013.

[28] M. Tafaoli-Masoule, a. Bahrami, and E. M. Elsayed, "Optimum design parameters and operating condition for maximum power of a direct methanol fuel cell using analytical model and genetic algorithm," *Energy*, vol. 70, pp. 643–652, jun 2014.

[29] D. E.Goldberg, *Genetic Algorithms in Search, Optimization and Machine Learning*. Addison-Wesley, 22 ed., 1989.

[30] L. Peerlings, *Methods and techniques for precise and accurate in-duct aero-acoustic measurements. Licenciate thesis*. No. 2015:25 in TRITA-AVE, 2015.

[31] H. W. Coleman and W. G. Steele, *Experimentation, Validation, and Uncertainty Analysis for Engineers: Third Edition*. Wiley, 3 ed., 2009.

[32] J. S. Bendat and A. G. Piersol, *Random Data*. Wiley, 4. ed., 2010.

[33] S. Allam, M. Åbom, and H. Bodén, "Over-determiantion in acoustic two-port data," *Icsv*, 2006.

[34] P. M. Morse, *Theoretical Acoustics*, vol. 38 of *International series in pure and applied physics*. Princeton University Press, 1970.

[35] C. Weng, *Theoretical and numerical studies of sound propagation in low-Mach-number duct flows*. PhD thesis, KTH, Linné Flow Center, FLOW, 2015.

[36] L. Feng, "Acoustic properties of Fluid-Filled Elastic Pipes," *Journal of Sound and Vibration*, vol. 176, no. 3, pp. 399–413, 1994.